Subcellular processes in morphogen gradient formation studied with 3D tracking fluorescence microscopy

Holtzer, L.H.F.M.

Citation

Holtzer, L. H. F. M. (2008, December 8). *Subcellular processes in morphogen gradient formation studied with 3D tracking fluorescence microscopy*. Casimir PhD series 2009-19, Delft-Leiden. Retrieved from https://hdl.handle.net/1887/14504

Version: Corrected Publisher’s Version

Chapter 4

Endosome motility and endosomal cargo dynamics mediate morphogen gradient formation

In the wing imaginal disc of *Drosophila melanogaster* positional information is provided by a concentration gradient of the morphogens Decapentaplegic (Dpp) and Wingless. Three transport mechanism govern formation and maintenance of the gradient. Here we focus on intracellular transport of Dpp. Using a 3D wide-field fluorescence microscope and particle tracking algorithms we were able to quantify the role of endosome mobility and endosomal cargo dynamics in intracellular Dpp transport.

We found that the lateral motility of endosomes by itself cannot account for effective intracellular transport. In the apicobasal direction however directed transport was observed during 6% of the time, with velocities that agreed with previously found values for molecular motors. The function of this endosomal transport remained unclear, but we speculate that it might play a role in Dpp degradation. We characterized the spatio-temporal endosomal Dpp distribution in the wing disc in all three dimensions *in vivo* and found it to be single-exponential, identical to the distribution of the complete Dpp population. The number of endosomes however remained constant throughout the disc. Endosomes contained up to 250 Dpp molecules allowing us to follow endosomes for hundreds of frames with high accuracy. Sudden changes in Dpp content of up to 25 Dpp molecules were observed, indicating that vesicles traveling between endosomes contain multiple Dpp molecules both before fusion with an endosome, and after fission from an endosome. The time between Dpp in- and outflow events was found to be about one minute. Dpp outflow was found to be a passive, probabilistic process. Combining these results suggested the presence of an immobile Dpp fraction, similar to what was observed with FRAP experiments before.

Our study is the first study to quantify intracellular Dpp transport on the level of individual endosomes. The results on the role of endosomal motility and endosomal cargo dynamics will have to be integrated in the future into a more detailed model describing intracellular Dpp transport.

4.1 Introduction

Almost 60 years ago Turing proposed that morphogens are providing the positional information in morphogenesis [1]. Wolpert in turn further developed a model in which morphogens are produced only by spatially localized cells. This then leads to the formation of a morphogen gradient in the surrounding 'receiving' tissue [2]. The position of a cell is hence coded into its position in a morphogen gradient. In the receiving tissue, the morphogen is detected by receptors on the cell surface. Depending on the morphogen concentration, cells will change their gene expression pattern accordingly. While the concept of morphogen gradients is now accepted for decades, the mechanism underlying the formation of these gradients on the cellular, sub-cellular and molecular level has only started to become understood in recent years. The formation of a stable gradient requires three mechanisms: production of the morphogen, spreading to neighboring cells and finally degradation of the morphogen.

In what follows we focus on morphogen spreading in tissue. For this process three mechanisms have been proposed: (i) diffusion in the extracellular matrix [3], (ii) receptor-mediated transport along the cell membrane [4] and (iii) intracellular transport [5], a sequential sequence of endocytosis of the morphogen-receptor complex followed by recycling and release of the morphogen into the extracellular matrix [6].

We studied the spreading of the morphogen Decapentaplegic (Dpp), a member of the TGF-β superfamily, which plays a major role in the development of the fruit fly *Drosophila melanogaster*. Dpp is expressed in a stripe of cells (the 'source') at the anterior-posterior compartment boundary (fig. 4.1a) of the wing imaginal disc [8]. The wing imaginal disc is a precursor of the later wing (fig. 4.1b). Figure 4.1c shows a schematic xz projection (a cross-section perpendicular to the dorso-ventral axis) of the wing imaginal disc consisting of two layers of distinct cells. The peripodial layer on top and the columnar cells beneath in which the Dpp gradient is present. The producing cells are indicated with a green bar in fig. 4.1c. From these producing cells Dpp is secreted to neighboring cells where it forms an exponential gradient in the wing epithelium [5, 9, 10]. In a recent experimental study of the Dpp gradient it was

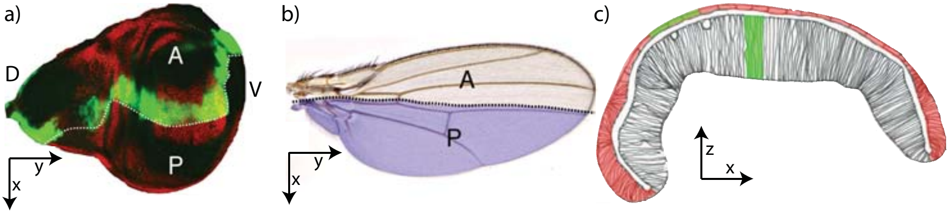

Figure 4.1: The wing imaginal disc. The x, y and/or z-axes are indicated in each subfigure. **a)** Top view of the wing imaginal disc showing the anterior (A) and posterior (P) compartment. The Dpp source (green) is located at the A-P compartment boundary. The dorsal (D) and ventral (V) sides are also indicated. **b)** Wing of a mature fly with the anterior and posterior compartment indicated. **c)** Schematic cross-section of a wing imaginal disc perpendicular to the D/V-axis. The Dpp source is indicated by the green color. (images from [5, 7])

shown that the formation of the gradient is a combination of Dpp production, Dpp spreading throughout the tissue and Dpp degradation within the cells as described by

$$\partial_t C(x,t) = D_{\text{eff}} \nabla^2 C - kC + 2j_0 \delta(x) \tag{4.1}$$

in which $C(x,t)$ is the Dpp concentration at time t and distance to the source x. With confocal fluorescence microscopy quantitative values for the effective diffusion coefficient D_{eff}, the degradation rate k and the production rate j_0 have been obtained [10]. While in the latter study the actual Dpp transport mechanisms were modeled with one effective diffusion coefficient D_{eff}, here we report on experimental findings that describe morphogen spreading by subcellular processes which finally lead to the effective coefficients and rates reported. Our experimental work is in line with ongoing theoretical efforts to describe Dpp spreading on the cellular and subcellular level [7, 11, 12].

4.1.1 Intracellular Dpp transport

Here we experimentally study the intracellular transport of Dpp in wing epithelia on the cellular and sub-cellular level by analyzing endosome motility

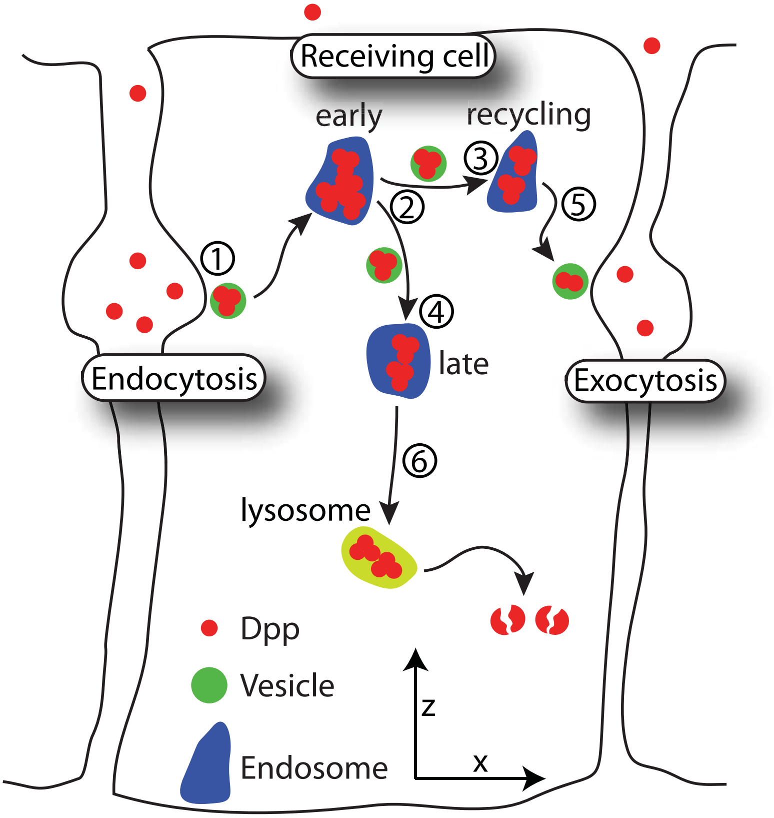

Figure 4.2: Schematic drawing of intracellular Dpp transport. Numbers indicate the different events that occur: **1)** Dpp endocytosis into a vesicle and concurrent fusion with an early endosome. **2)** Fission of a vesicle containing Dpp from an early endosome. **3)** The vesicle from (2) going to a recycling endosome. **4)** The vesicle from (2) going to a late endosome. **5)** Fission of a vesicle from a recycling endosome and concurrent exocytosis. **6)** Fission of a vesicle from a late endosome to a lysosome. Intracellular Dpp transport is non-directional. Any directionality of Dpp transport as suggested in this figure is for clarity purposes only.

and monitoring the concentration of Dpp in endosomes. Intracellular Dpp transport plays a major role in gradient formation. This idea is supported by experiments in which intracellular Dpp transport was selectively blocked within part of the tissue by locally defined genetic shut down of endocytsosis [5]. The intracellular transport of Dpp is schematically shown in fig. 4.2. In this model we distinguish different events [1]:

1. Endocytosis of Dpp into a vesicle with concurrent fusion of this vesicle with an early endosome (+).
2. Fission of a vesicle containing Dpp from an early endosome (-)
3. after which it can go either to a recycling endosome (+)
4. or into a late endosome (+).
5. Fission of a vesicle containing Dpp from a recycling endosome and concurrent recycling of the Dpp into the extracellular matrix (-).
6. Fission of a Dpp-containing vesicle from a late endosome to a lysosome for degradation (-).

Such sequential processes are best described in terms of a system of rate equations in which a change in endosomal Dpp concentration dC is related to a rate k_i and the Dpp concentration c_i in the vesicle that is involved in process i. The change in concentration for each endosome is described by:

$$\partial_t C_{\text{early}} = c_1 k_1 - c_2 k_2 \tag{4.2a}$$

$$\partial_t C_{\text{recycle}} = c_3 k_3 - c_5 k_5 \tag{4.2b}$$

$$\partial_t C_{\text{late}} = c_4 k_4 - c_6 k_6 \tag{4.2c}$$

---

[1] For each event it is indicated in parenthesis if the Dpp concentration in the specified type of endosome increases (+) or decreases (-). For each event the corresponding number is indicated in fig. 4.2.

Further we identify from fig. 4.2 that a vesicle that originates from an early endosome (event 2) will transfer either to a recycling endosome (event 3) or a late endosome (event 4). As the Dpp concentration in this vesicle will not change during these events (2→3 or 2→4) $c_2 = c_3 + c_4$. Knowledge of the parameters involved in the coupled differential equations will provide us with the full description of intracellular Dpp transport.

Theoretical calculations have estimated that one cycle of intracellular transport has a duration between 50 and 150 s [6, 13]. In a companion study to the current one we determined rates k_2 and k_5 of the events described above using Particle Image Cross-Correlation Spectroscopy (PICCS, chapter 3). By labeling both Dpp and early endosomes we estimated the off rates for the 'fission' events by determining the cross-correlation between both populations using the PICCS algorithm.

Much of the previous work on Dpp gradients has been done with conventional fluorescence microscopy. Here we build on our expertise in the field of single-molecule wide-field fluorescence microscopy [14, 15] which has distinct advantages over confocal microscopy in imaging speed and sensitivity and allows for straightforward determination of the Dpp concentration in endosomes. While in the companion study we focused on the kinetic parameters for Dpp transport, here we study how intracellular transport is actually facilitated. In particular we investigated:

1. Do endosomes or the vesicles travelling between endosomes control Dpp transport?
2. What are the other roles of endosomes we see?
3. Do Dpp molecules travel individually or in clusters during intracellular transport?
4. Is there evidence for directionality in intracellular transport?

By employing single particle tracking methods we studied all those questions and developed a quantitative description of intracellular Dpp transport on the level of individual endosomes.

4.2 Materials and methods

4.2.1 Sample preparation

The *UAS-Venus-Dpp* line was generated by using the existing *UAS-GFP-Dpp* vector [5] where GFP was replaced by Venus [16]. *dpp*^{d8}/*dpp*^{d12}; *dppGal4/UAS-Venus-Dpp* flies have an identical wing phenotype to the *dpp*^{d8}/*dpp*^{d12}; *dppGal4/UAS-GFP-Dpp* flies [5]: they survive to adulthood and have normally patterned wings, although smaller in size (data not shown). To obtain wing imaginal discs third instar larvae (*dpp-Gal4/UAS-Venus-Dpp*) were dissected in Clone8 medium (Schields & Sang M3 Medium containing 2% Fetal Calf Serum, 2.5 % Fly Extract, 12.5 IU Insulin/100 ml medium and 1X Penicillin/Streptomycin) after which the wing imaginal discs were mounted in a custom-made sample holder. Nail polish was used for sealing of the sample holder. The wing imaginal discs were imaged approximately 10 min after dissection. Samples were discarded 1 hour after dissection.

4.2.2 Data acquisition

A transmission image of a wing imaginal disc is shown in fig. 4.3a. When the sample is excited by a mercury lamp (excitation in the 500-520 nm range) the fluorescence from the DppVenus is clearly seen (fig. 4.3b). Magnification of the source area shows endosomes containing Dpp (fig. 4.3c). After addition of low concentrations of the membrane marker FM4-64 (Invitrogen, Leiden, The Netherlands) to wing disc during preparation, both the Dpp-Venus fluorescence (fig. 4.3c, $\lambda < 600$ nm) and the cell membranes (fig. 4.3d, $\lambda > 600$ nm) become visible. Overlaying both images (fig. 4.3e) allows us to assign each endosome to a specific cell.

Experiments were carried out on a wide-field fluorescence microscope capable of three dimensional particle-tracking through astigmatism [17]. The setup was additionally combined with a piezo-driven objective holder (Physik Instrumente, Karlsruhe, Germany) to move the objective in axial direction at 10 nm-precision. A motorized sample stage (Märzhäuser, Wetzlar, Germany)

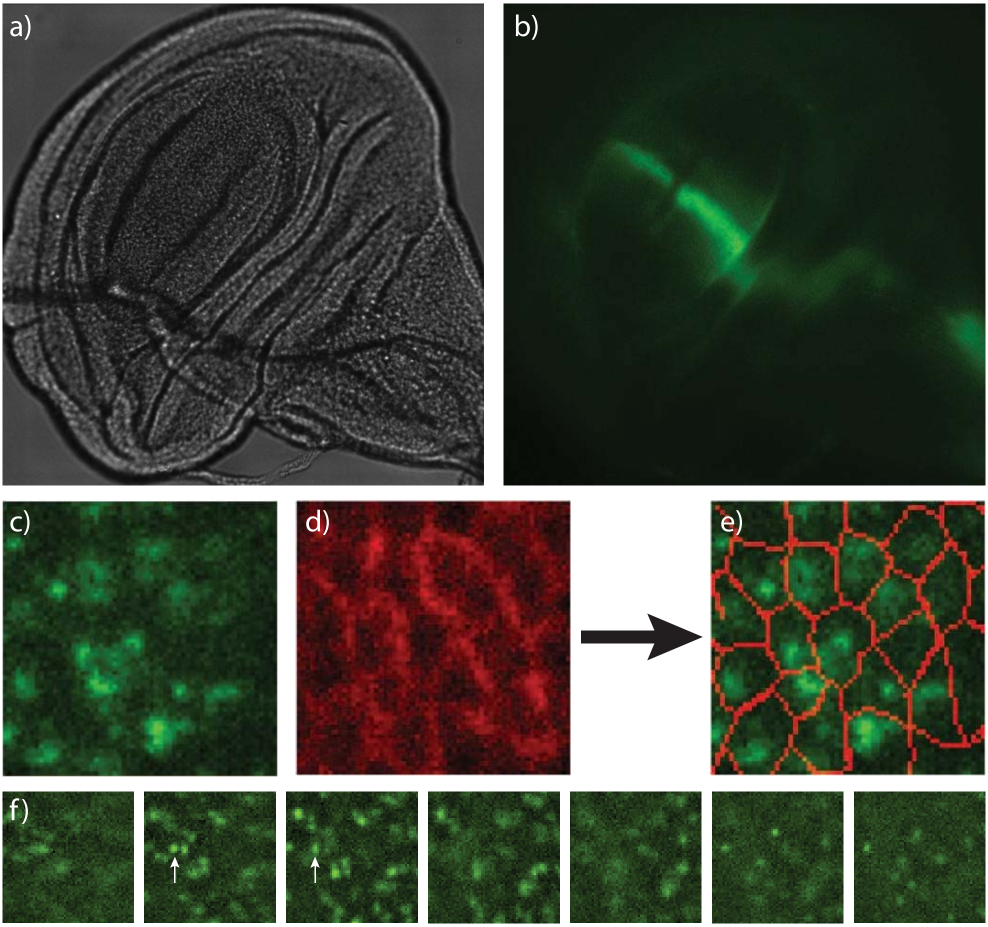

Figure 4.3: **a)** Transmission image of a wing imaginal disc directly after dissection. **b)** The same wing imaginal disc, now excited by a fluorescent lamp (500-520 nm). Dpp-Venus can be clearly seen, especially in the Dpp producing cells. The location of the Dpp source is indicated, together with the anterior-posterior compartment boundary which marks the border between producing and receiving cells. In the receiving cells a gradient is observed. **c)** A close-up of the receiving cells, individual Dpp-containing endosomes can be clearly seen. **d)** The same area as in (c), but now imaged in the red channel, showing the fluorescence of membrane-marker FM4-64, clearly outlining the columnar cells. **e)** Merge of images (c) and (d). **f)** Typical data obtained during an experiment in one image stack. Each image corresponds to a different z-position going from very apical (left image) to more basal (right image) with a distance of 0.7 µm between the planes. Out-of-focus fluorescence is removed in these images for clarity.

was used to move the sample in lateral direction with sub-micrometer accuracy. Image stacks with 5 to 8 image planes were generated in order to image large volumes. The distance between planes was set between 0.7 and 1.0 µm such that endosomes appeared in at least two planes. The time between planes was kept as short as possible (typically 40 ms) to prevent large movements of endosomes between planes, while allowing enough time for the piezo to move the objective. Imaging was done in the apical region of the wing imaginal disc. A typical image stack is shown in fig. 4.3f, where 7 planes with Δz = 0.7 µm were imaged. Endosomes containing Dpp-Venus were clearly identified in at least two images at the same time. The movement of endosomes between two consecutive planes was negligable. The astigmatism introduced for 3D position determination is visible in the images (see the endosome indicated by the white arrows in fig. 4.3f).

4.2.3 Data analysis

Positional information of endosomes was obtained as described before [17]. The method of fitting elliptical 2D-Gaussian profiles to the image of a single particle was extended here to incorporate image stacks. A stack of elliptical 2D-Gaussians was simultaneously fitted to the data, effectively producing a 3D-Gaussian profile. From this fitting procedure we obtained a static characterization for each experiment. A typical analysis output is shown in fig. 4.4. Each graph summarizes data from all endosomes detected during one experiment at all time points. Figure 4.4a shows the distribution of the local background for each endosome in the first image stack. This is a measure for the out-of-focus fluorescence. The background has a mean value of 625 ± 20 cnts, with a standard deviation of 117 cnts. This value is much smaller than the average signal observed from an individual endosome of $\overline{I} = 8.6 \pm 0.8 \cdot 10^3$ cnts, with a standard deviation of $4.4 \cdot 10^3$ cnts, as shown in fig. 4.4b. A wide range of intensities was observed in this experiment, reflecting the differences and changes in the Dpp concentration in endosomes and photobleaching of the Dpp-Venus.

The black curve in fig. 4.4b shows the intensity distribution for single YFPs attached via a membrane anchor to human embryonic kidney cells [18]. The

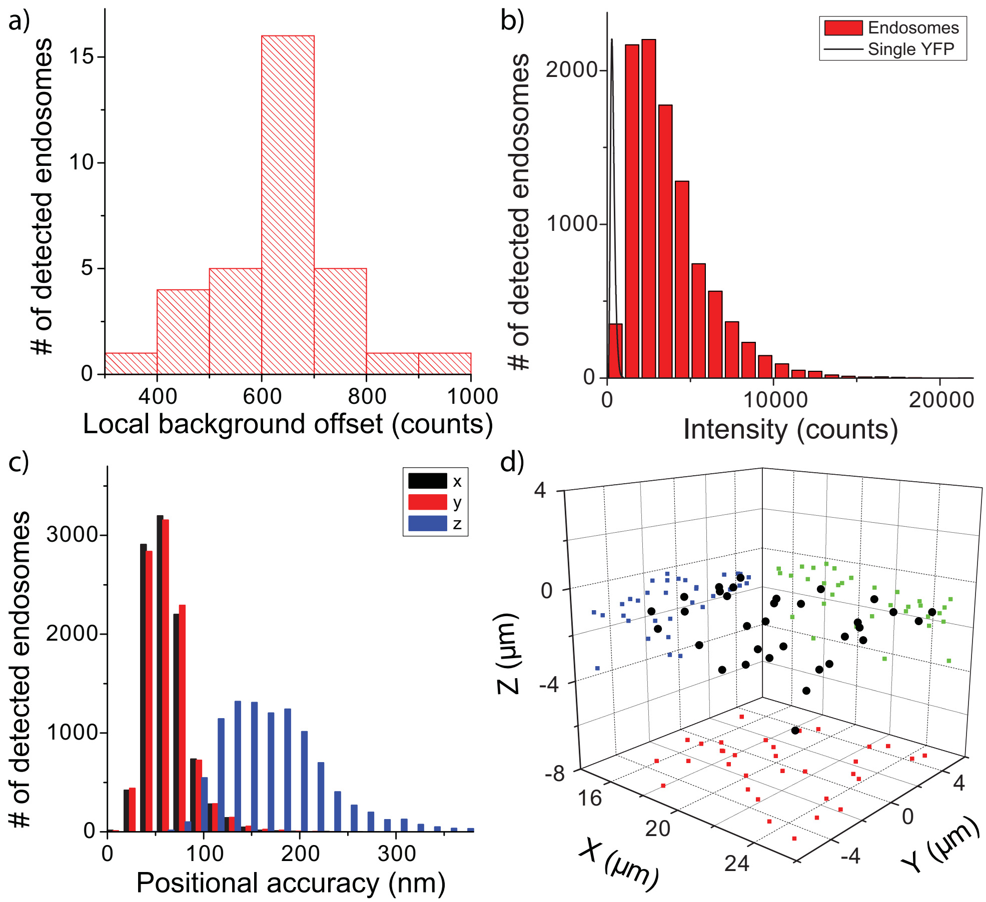

Figure 4.4: Typical output of the initial data analysis of a single experiment. **a)** Distribution of background values (CCD counts) associated to each detected endosome in the first image stack of the experiment. **b)** Distribution of all intensities for every endosome detected during the whole experiment (bar plot). For this plot each image stack is treated individually and therefore one endosome appearing in multiple image stacks will contribute multiple data points to this plot. The intensity distribution of single YFP proteins is plotted (black line) and the intensity is scaled for better comparison with endosome intensities. **c)** Distribution of the positional error for localizing an endosome for each dimension (x in black, y in red and z in blue), again for the whole experiment. **d)** Location in x (distance to the source), y and z for each detected Dpp endosome in the first image stack.

distribution peaked at 281 cnts. This distribution was already corrected for the different exposure time and excitation intensity used in the Dpp experiments. In doing so we assumed that the fluorescence intensity of YFP scales linearly with both parameters, since both experiments were performed in the non-saturating regime for YFP (excitation intensity $I_{\mathrm{ex}} = 0.1\,\mathrm{kW/cm^2}$ was far below the saturation intensity [19]). Furthermore we assumed that quenching of fluorescence does not play a significant role inside the endosome given that the average distance between Dpp molecules in a 400 nm diameter endosome containing 100 Dpp molecules is approximately 80 nm.

To be able to calculate the number of Dpp molecules in an endosome it was necessary to correct the measured endosome signal for photobleaching. This was done by calculating a photobleaching curve for each experiment from the average signal per detected endosome and image stack for an entire movie. The fact that there were a large number of endosomes (> 15) in each image stack rendered this strategy reliable. We found that DppVenus bleached following a bi-exponential decay with offset as reported earlier by others [20]. The bleaching curve was subsequently fitted to a bi-exponential decay, the parameters obtained in this way (typical values $\tau_1 = 7$ images, $\tau_2 = 244$ images, offset = 2000 counts) were further used to correct the intensity of each individual endosome in retrospect.

To determine Dpp concentration changes in endosomes we used a step-fitting algorithm developed by Kerssemakers et al. [21]. We decided for the latter algorithm as it directly accounts for noise and no pre-filtering of the data is needed (for a review of other algorithms see [22]). Small steps of a few Dpp, however, were difficult to observe due to the unavoidable background fluorescence present in tissue. Furthermore, since photon shot noise has a bandwidth of a few Dpp, small changes on short time scales were not detected.

The positional accuracy by which the x, y and z coordinates of each endosome were determined is shown in fig. 4.4c. Since the positional accuracy is inversely proportional to the square root of the number of detected photons, endosomes with more Dpp were detected more accurately. Photobleaching slightly reduced positional accuracy. As shown before the positional accuracy in axial direction $\Delta z = 172$ nm is approximately 2.5 times that in lateral direction $\Delta x = \Delta y = 64$ nm [17]. Finally fig. 4.4d shows the positions of the detected endosomes during the experiment showing that most of the endosomes where located in an apical slice of 4 µm at about 1 µm inside the tissue. After locating the endosomes in each image stack, endosome trajectories were reconstructed by using a particle tracking algorithm that has previously been described [14, 17]. With this approach the 3D position of each endosome as well as its Dpp content was followed for a long period (up to 600 time points).

Trajectories were further analyzed [23] in order to detect different types of motional behavior for each endosome. Free diffusion was classified against confined diffusion and against directed transport. For parts of trajectories were free diffusion was detected, a mean squared displacement (MSD) versus time plot was generated from which the diffusion coefficient D was calculated

$$\mathrm{MSD} = 2nDt + \sum 2\sigma_n^2 \tag{4.3}$$

in which n is the dimensionality of the data and σ_n the positional accuracy in the nth dimension. To locate parts of a trajectory where directed motion is occurring an 'asymmetry' parameter was calculated following the methodoogy described by [23]. The trajectory of a transported object will be highly asymmetric, showing up as an asymmetry parameter larger than 1. As argued by [23] this value is indicative of a probability > 99% that the object undergoes directed motion. After analysis of the asymmetry parameter, in the case of directed transport, the MSD versus time plot was calculated on the part of the trajectory where asymmetry > 1 and fitted to

$$\mathrm{MSD} = 2nDt + (vt)^2 + \sum 2\sigma_n^2 \tag{4.4}$$

from which the average velocity v of the endosome during the transport period was obtained [24].

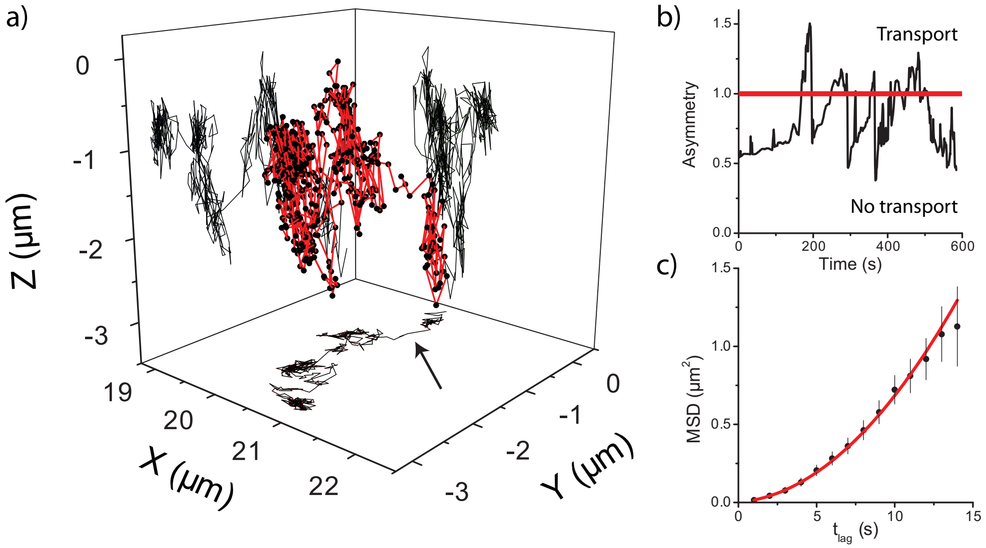

Figure 4.5: **a)** Trajectory (total length = 600 s) of an endosome undergoing transport in the lateral direction during a short period (15 s). The distance to the Dpp source is indicated on the *x*-axis. **b)** Three-dimensional asymmetry parameter of the trajectory versus time. Values above 1 indicate a high probability that directed motion is occurring. **c)** Mean squared displacement versus time lag for the part of the trajectory indicated with the arrow. From a fit to eq. (4.4) we found that the endosome was transported with an average velocity $v = 78 \pm 20$ nm/s.

4.3 Results-Endosome mobility

4.3.1 Intracellular transport by endosomes

The simplest form of intracellular transport would be endocytosis of Dpp, followed by a short period of transport or diffusion through the cytosol and subsequent exocytosis. During a typical experiment with a duration of 600 s we expected these events to be frequently observable given that the estimated time of intracellular transport lies between 50 s and 150 s [6, 13, 25]. In particular, our experiments were intended to unravel whether intracellular transport was mainly diffusion-driven or whether it was directional.

Previous experiments suggested that on macroscopic length scales intracellular transport was non-directional [5]. Indeed, on the (sub)cellular level we did not observe any significant long-range endosome transport over the whole width of a single cell (typical cell diameter 2.6 μm). In total 48 wing-disc preparations were analyzed, of which 15 preparations contained trajectories of a satisfactory quality (no significant sample drift and endosomes were visible during the whole experiment). Each experiment provided between $5 \cdot 10^3$ and 10^4 endosome positions of which typically around 200 endosome trajectories were obtained with average length of 25 steps (exponentially distributed). Of those, trajectories of lengths > 30 steps ($\Delta t > 30$ s) were further analyzed (typically $10 < N < 60$ for one experiment). One wing imaginal disc (on average 17 cells were visible in our experiments) was analyzed more thoroughly for endosome motility and we found that only 14% of long trajectories covered the whole diameter of a cell, and that this movement took significantly longer than 150 s.

As an example of this movement, fig. 4.5a shows an endosome trajectory of length 600 s showing clear directed transport in the xy-plane on a length scale that matched the typical cell size. From the three-dimensional asymmetry parameter (fig. 4.5b) it became clear that the endosome underwent directed transport in parts of its trajectory. For one of those stretches lasting for $\Delta t = 15$ s the two-dimensional (xy) MSD was calculated (fig. 4.5c.) From a fit to eq. (4.4) the average lateral velocity by which this endosome was trans-

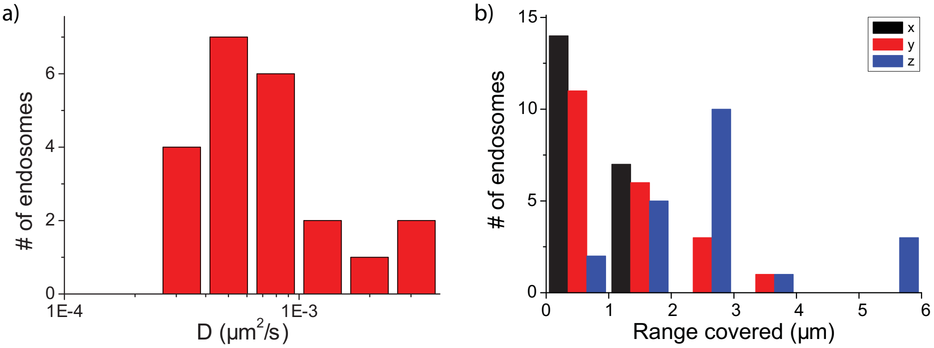

Figure 4.6: **a)** Distribution of two-dimensional (xy) diffusion coefficients D for Dpp-containing endosomes. **b)** Distribution of the range in which each endosome moves. For each dimension (x (along the gradient), y (perpendicular to the gradient), z (apicobasal)) the range is plotted. Endosomes clearly were more mobile in axial as compared to lateral direction.

ported was $v = 78 \pm 20$ nm/s. This value is lower than what is typically found in comparable systems [26, 27]. Hence, although we found trajectories which could account for directed transport, the fact that we observed only few of these events and that the observed velocities were low, rules out that they are the main mediators of intracellular Dpp transport. In general we therefore rule out that the motion of endosomes is facilitating intracellular transport or is causing directionality herein.

For non-directional intracellular transport, endosomes do not need to cover the whole diameter of a cell. They could travel from one position, close to the cell membrane, to a random other one, either by diffusion or directed transport and carry Dpp along with them. Here we analyzed whether diffusion of endosomes was sufficient to play a role in intracellular Dpp transport. Therefore we calculated the two-dimensional MSD versus time lag for each endosome. We estimated the two-dimensional (xy) diffusion coefficient D by fitting eq. (4.3) to the data for $1\ \text{s} \leq t_{\text{lag}} \leq 25\ \text{s}$ for each individual endosome. The measured distribution of diffusion coefficients is shown in fig. 4.6a. The mean diffusion constant which characterizes endosome transport was $\langle D \rangle =$

$8.9 \pm 1.5 \cdot 10^{-4}$ µm^2/s. If we however do not take into account the endosome population which covered the range of a whole cell during the experiment (14%) we obtain $\langle D \rangle = 6.9 \pm 1.0 \cdot 10^{-4}$ µm^2/s. For the upper limit (150 s) for intracellular Dpp transport an endosome would cover on average an area of 0.4 µm^2 or a typical distance of 0.6 µm. For effective intracellular transport this value is on the low side when compared to the cell diameter, also since most of the endosomes were usually not close to the cell membrane. Therefore we rule out here that mobility of whole endosomes will govern or facilitate intracellular Dpp transport.

4.3.2 Axial endosomal movement

So far we addressed lateral (xy) motion of endosomes. In what follows the axial (z, along the apicobasal axis) movement will be further evaluated. Since the observed lateral diffusion coefficients were small and lateral movement was small compared to the cell diameter, we did not expect to see a difference between lateral and axial movement. Lateral movement was even so small that during the timeframe of our experiments (t=600 s) we did not observe any influence of the cell membrane and we did not find lateral confinement with the size of the cell diameter. In fig. 4.6b a histogram is plotted showing the distribution of ranges each endosome covered during the experiment. The average covered range in x and y is 0.76 ± 0.09 µm and 1.1 ± 0.2 µm, respectively. In z the average range covered by an endosome equals 2.5 ± 0.3 µm, more than twice the range for lateral movement. Hence we found a clear difference between lateral movement and movement along the apicobasal axis.

In fig. 4.7a a trajectory from an endosome showing preliminar apicobasal directed motion is plotted. From the yz and xz projections it was clear that the range of movement of the endosome in z was larger than in lateral directions. From the asymmetry parameter (fig. 4.7b) several periods of directed transport were detected. For one of these periods, indicated with an arrow in fig. 4.7a the MSD versus time plot is shown in fig. 4.7c. During that period the endosome was transported at an average velocity $v = 283 \pm 32$ nm/s. This value is well in the range of velocities observed for intracellular transport by molecular motors

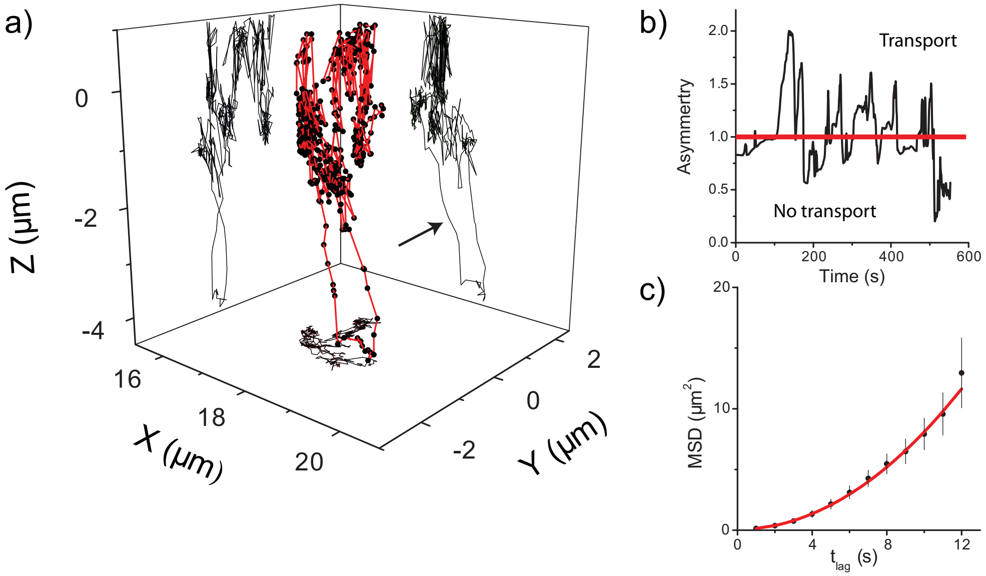

Figure 4.7: **a)** 3D trajectory of a Dpp-containing endosome showing movement in x, y and z. **b)** Asymmetry parameter of the trajectory shown in a). **c)** MSD versus time plot of the part of the trajectory indicated with the arrow. Directed transport was observed for 12 s and the endosome had an average velocity $v = 283 \pm 32$ nm/s.

[26, 27]. Therefore we assume that this particular endosome was transported by molecular motors during a period of 12 s thereby traveling a distance of 3.4 µm. We excluded the possibility that the tissue as a whole was moving in axial direction, since the axial movement of the other observed endosomes was not correlated to the axial movement of the endosome shown in fig. 4.7.

We analyzed all long trajectories in this wing imaginal disc (N=27 trajectories) according to the methodology delineated in fig. 4.7. Figure 4.8a shows the distribution of axial velocities for directed transport events, characterized by an average of $\overline{v_z} = 212 \pm 13$ nm/s. Thereby axial transport lasted between 3 s and 15 s with average duration of 7.6 ± 0.4 s (fig. 4.8b). It should be noted that short (< 3 s) periods of transport were not detected due to the temporal threshold that had to be introduced into the trajectory analysis algorithm. Likewise slow movements (< 50 nm/s) were not reliably detected if they occurred over short periods of time. Averaged over periods of transport, during single transport events endosomes travelled in axial direction by 1.4 ± 0.1 µm (fig. 4.8c). When we summed the duration of all the periods of directed transport, we found that in 6% of the time endosomes were clearly transported in the z-direction.

If all directed transport events were independent of each other, the distribution of the time between events is expected to peak around 124 s (i.e. equal to the total time without directed motion divided by the number of detected directed motion events). Our data however showed a completely different distribution, as shown in fig. 4.8d. In 56% of the cases transport in the z direction (either apical or basal) was followed by transport in the opposite direction within 17 s. In 32% of the cases reversal of transport is almost instantaneous. Such a large fraction of trajectories showing fast reversal of the direction of transport cannot be a result of random events. These events were most likely actively driven and therefore correlated.

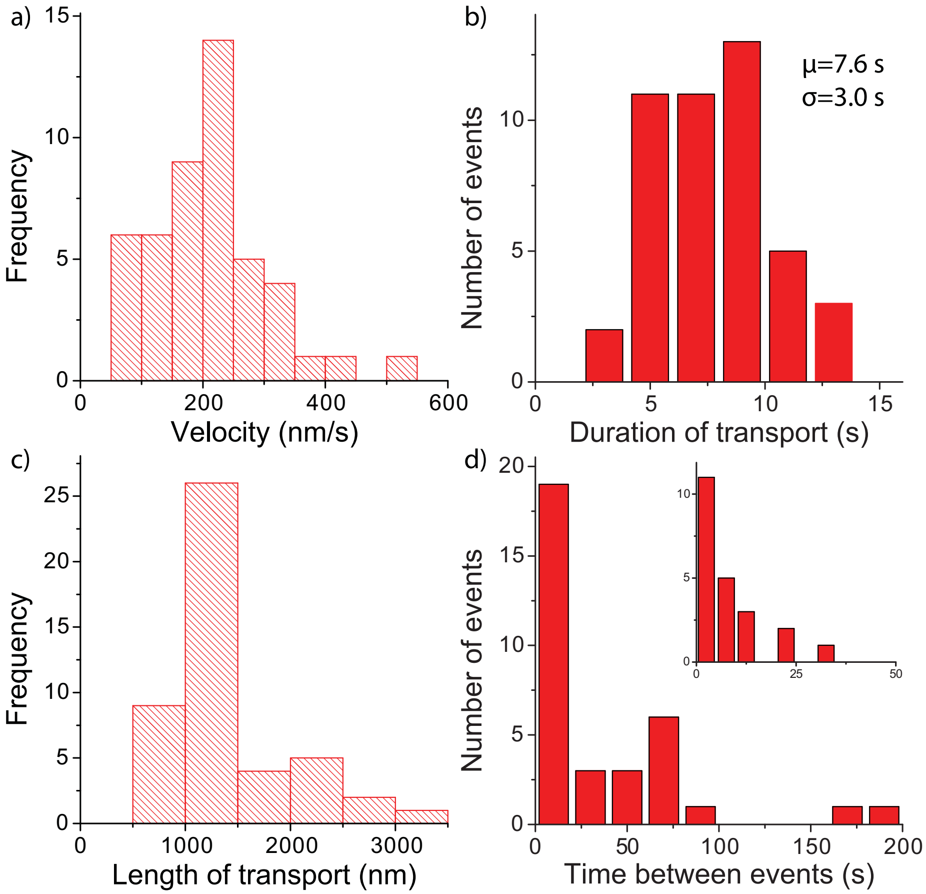

Figure 4.8: Directed transport statistics for multiple endosomes showing data from all the parts of the endosome trajectories where directed transport in the axial direction (along the apicobasal axis) was observed. **a)** Distribution of velocities. **b)** Distribution of duration of the detected directed motion, with an average $\mu = 7.6$ s and standard deviation $\sigma = 3.0$ s. **c)** Distribution of total distance covered by each transport event. **d)** Distribution of the time between transport events. The inset shows a zoom of the histogram for the data where time between events < 50 s.

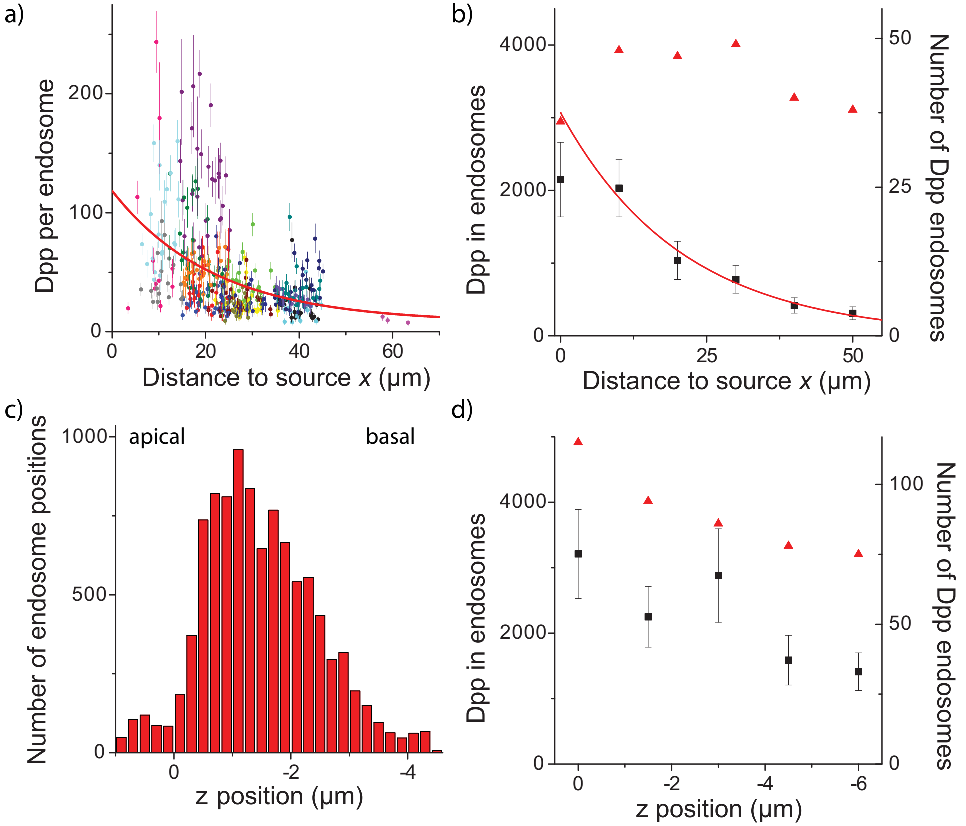

Figure 4.9: **a)** Amount of Dpp molecules per endosome plotted versus the distance to the source. Different colors indicate different wing imaginal discs. Fit of a single exponential to the data gives a decay length $\lambda = 22 \pm 9$ µm. **b)** Total number of Dpp molecules (black squares) and number of Dpp endosomes (red triangles) in a volume of 10x10x5 μm^3 versus source distance for one wing imaginal disc ($\lambda = 20.8 \pm 3.4$ µm). **c)** Apicobasal distribution of Dpp endosomes in the wing imaginal disc. All positions of the detected endosomes in each image stack from an experiment are binned together. The apical edge of the columnar cells is defined as $z = 0$ µm. **d)** Apicobasal distribution of Dpp molecules (black squares) and number of Dpp endosomes (red triangles) for the same disc as in **b)**.

4.4 Results-Dpp content of endosomes

4.4.1 Static characterization

The Dpp gradient was measured in wing imaginal discs (N=28) by locating Dpp-containing endosomes relative to the source and determining their Dpp content (fig. 4.9a). Each sample is indicated with a different color, showing the large heterogeneity between different discs. On top of large inter-sample heterogeneity, the number of Dpp molecules per endosome varied enormously within one disc. In one imaginal disc Dpp content was found to be ranging from 21 to 244 Dpp per endosome, a variation of one order of magnitude. Despite this heterogeneity the single-exponential nature of the gradient was visible.

Fitting a single exponential decay to all data in fig. 4.9a (number of endosomes > 500) gave a gradient of decay length $\lambda = 22 \pm 9$ µm, agreeing well with previous experiments where $\lambda = 20.2 \pm 5.7$ µm was found [10]. The average amount of Dpp per endosome at the source (C_0) was determined to be 110 ± 10 Dpp molecules.

To remove the effect of inter-sample heterogeneity the amount of Dpp in only one imaginal disc was measured as a function of the distance to the source (fig. 4.9b, black squares). Images were taken at intervals of 10 µm and all detected Dpp was summed. The data was fitted to a single-exponential (omitting the data point at $x = 0$ µm, since the image at that point contained both the Dpp-producing cells as well as the Dpp-receiving cells). The gradient has a decay length $\lambda = 20.8 \pm 3.4$ µm, which again agrees nicely with previously obtained results.

In the following we analyzed the data in more detail to unravel which underlying property was the source of the Dpp gradient. The observed single-exponential gradient can arise in three different ways:

1. The concentration of Dpp per endosome is constant and the number of endosomes per cell decreases further away from the source;

2. The opposite, i.e. a constant number of endosomes per cell and a de-

creasing amount of Dpp per endosome versus distance to the source;

3. A combination of 1 and 2.

From a biological point of view (1) seems to be unlikely, since the function of endosomes is not limited to collecting and transporting Dpp. A decrease of number of endosomes further away from the Dpp source would therefore also affect other cellular processes which involve endosomes. The same reasoning qualifies option (3) also as less likely. Furthermore a combination of changing the Dpp concentration and the number of endosomes seems to be a complex way to establish a single-exponential gradient. We therefore predicted that mechanism 2 will be the most likely mecahnism of gradient formation.

We confirmed this experimentally by measuring the average number of detected Dpp-containing endosomes versus distance to the source for the same wing disc as was used before (fig. 4.9b, black squares). The result is plotted in fig. 4.9b (red triangles). Our data show that over a large range (Δx = 19 cells) the number of detected Dpp endosomes stays constant (44 ± 2 Dpp endosomes per 500 μm^3). While previous experiments have shown the presence of a gradient for the whole Dpp population, our results demonstrated that also the endosomal Dpp subpopulation (85% of total Dpp population [10]) faithfully reflects the morphogen gradient, while the number of endosomes that contain Dpp does not change with distance to the source.

Besides the lateral distribution of Dpp we further studied the apicobasal distribution of Dpp endosomes and of Dpp itself. Previously it has been found that most of Dpp is located in the most apical 5 μm of the wing epithelium [5, 10]. We confirmed this by imaging the most apical 25 μm of the wing epithelium (data not shown). For one experiment (600 image stacks, lateral size = 10x10 μm^2, axial size = 5 μm.) the distribution of the z-positions of all detected endosomes during the movie were plotted in fig. 4.9c. In this experiment the majority of the endosomes were clearly confined to a layer of 3 μm within the tissue. In fig. 4.9d the apicobasl distribution of Dpp (black squares) and the apicobasal distribution of Dpp endosomes (red triangles) is shown for the most apical layer of 5 μm of the wing disc (distance to the source ranges from 0 μm till 50 μm). We again observed that the amount of Dpp is largest at the most apical side of the cell and decreases basally. Interestingly, also the amount of Dpp endosomes was largest in the most apical part of the cell. The relative decrease of the number of Dpp endosomes however is smaller than the relative decrease of the amount of Dpp. Therefore the average amount of Dpp per endosome is also the highest close to the apical membrane and decreases basally.

4.4.2 Dynamic characterization

As was shown before (fig. 4.5a & fig. 4.7a) Dpp-containing endosomes were followed for up to 600 frames for endosomes with high (>100 Dpp molecules) Dpp content. Such trajetories allowed us to study the fluctuations in the fluorescence signal of individual endosomes. The signal is taken as direct measure for changes in the Dpp concentration in the endosome. However, due to photobleaching, the fluorescence intensity of each endosome will decrease over time which in turn would translate into an apparent reduction of Dpp molecules in the endosome. Hence, to correct for photobleaching we measured for each experiment the average intensity per endosome for every time point, as shown in fig. 4.10a. A bi-exponential decay was subsequently fitted to the data and the curve obtained was in turn used to correct the intensity profile for each individual endosome in retrospect.

Figure 4.10b shows the Dpp content of the endosome versus time in a living wing disc (blue curve) and in a fixed wing disc (red curve) in which supposedly no dynamics took place. For the fixed sample the 2σ confidence interval level for the noise is shown (dashed area) which arises from both photon shot noise (50 % of total noise) as from sources in the sample itself (out-of-focus fluorescence). For the experiment in the live wing disc, data were treated accordingly. In contrast to the data on the fixed wing disc the observed fluctuations clearly fall outside of the 2σ interval and cannot be purely explained by noise. Figure 4.10c and fig. 4.10d show the distribution of the measured intensities for the fixed and the living wing disc endosome, respectively. As predicted, the intensity distribution for the fixed wing disc endosome was fully described by

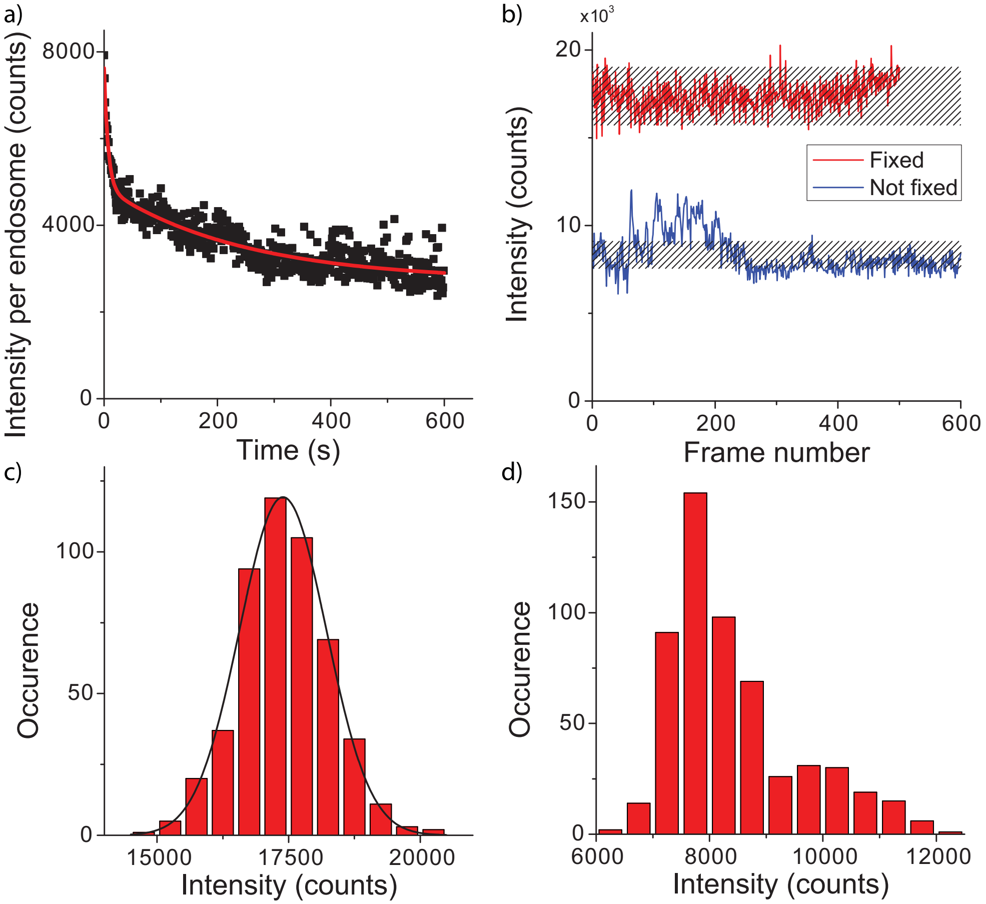

Figure 4.10: **a)** Average intensity per endosome for each image stack. A bi-exponential is fitted to the data and this curve is used to correct the intensity profile of individual endosomes in this experiment. **b)** The intensity of two endosomes plotted versus time and corrected for photobleaching. The red curve shows data from an endosome from a wing disc in which all material was fixed. The blue curve shows the intensity of an endosome from a live wing disc (not fixed). The expected noise in the intensity is indicated by the dashed area. **c)** Histogram of the intensity values of the data from the fixed endosome in (b). As expected the shape of the histogram is Gaussian, and thus the intensity fluctuations are fully explained by noise. **d)** Histogram of the intensity values of the data from the not-fixed endosome in (b). The shape of the histogram is clearly non-Gaussian, indicating that the intensity fluctuations cannot only be explained by noise.

a Gaussian with $\mu = 17392 \pm 25$ counts and $\sigma = 827 \pm 25$ counts.[2] The intensity distribution for the non-fixed endosome however, could not be described by a simple Gaussian distribution, supporting the conclusion that the fluctuations are not purely caused by noise, but by Dpp dynamics. Since the noise level in all experiments was on the order of a few Dpp molecules (depending on the total intensity) we conclude that our experimental setup was sensitive enough to directly observe in- and outflow of Dpp from endosomes in small packages of Dpp.

As explained before (section 4.1.1) changes in Dpp concentration in an endosome occur when a vesicle containing Dpp fuses with an endosome (up steps) or when Dpp is removed from an endosome (down steps), see fig. 4.2. By collecting many trajectories of endosomes and their Dpp-concentration profiles we obtained distributions of C_{endo}, k_i and c_i. These distributions were subsequently used to make a detailed quantitative description of events in intracellular Dpp transport. It should be noted that in this analysis we could not segment the endosomes according to their type (i.e. early, recycling or late) and the obtained distributions will therefore represent multiple underlying events.

To determine if the events in intracellular transport as described in section 4.1.1 are involving individual Dpp molecules or clusters of Dpp we studied the size of the changes in Dpp concentration for each endosome. For this purpose we obtained Dpp concentration profiles for each individual endosome (an example is shown in fig. 4.11a) and subsequently used a step-fitting algorithm [21] to determine the step size of each event. This has been done for many different endosomes, resulting in 179 'step'-events, the distribution of step sizes is shown in fig. 4.11b. From the result it became clear that both in- and outflow events usually involve clusters of Dpp, with 97% of the events having a Dpp cluster size of 25 or less.

To determine if there was a difference between the Dpp cluster size for Dpp in- or outflow we calculated the average cluster size for both groups. For up-steps we found $\langle \Delta c_{\text{in}} \rangle = 8.5 \pm 1.1$ Dpp and for down-steps $\langle \Delta c_{\text{out}} \rangle = 6.6 \pm 0.6$

---

[2] Although shot noise is Poissonian distributed, it can be approximated by a Gaussian distribution for large values

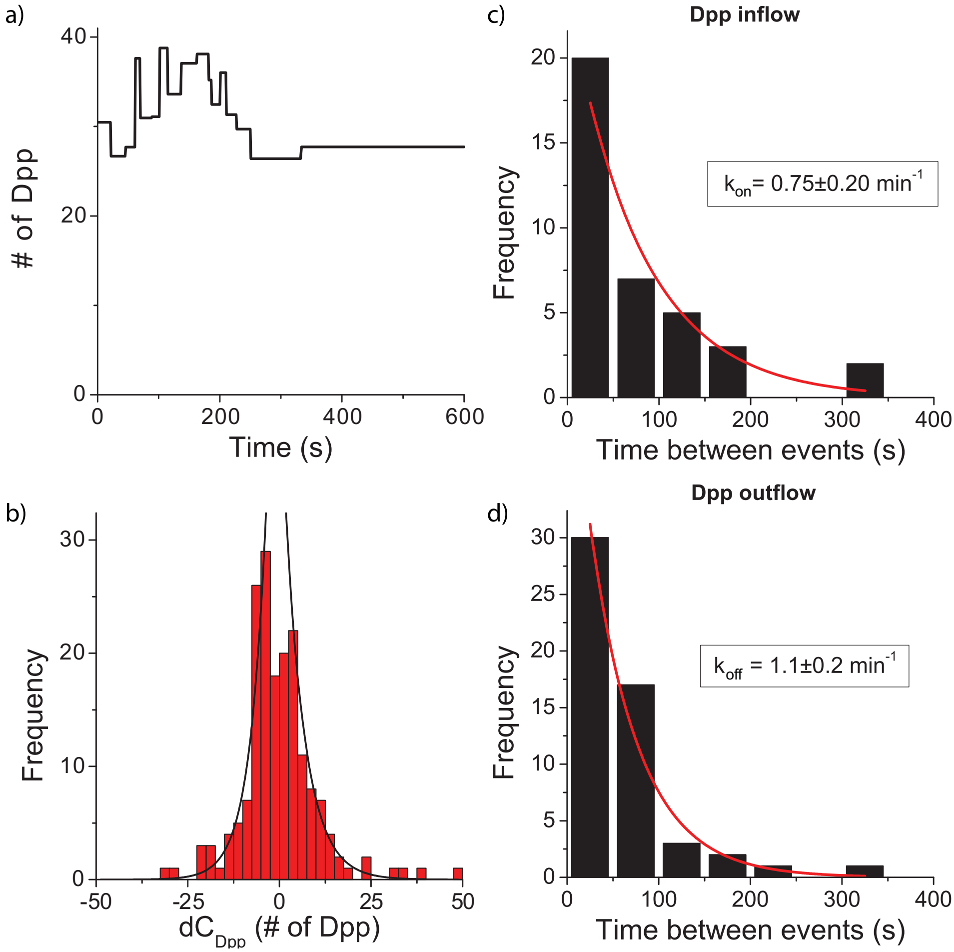

Figure 4.11: **a)** Intensity of a Dpp endosome versus time (black line). The green line shows the result of the applied step-fitting algorithm [21]. **b)** Distribution of step sizes independent of distance to the Dpp source. The size of Dpp steps seems to be exponentially distributed with an average of $\langle \Delta c_{\mathrm{in}} \rangle = 8.5 \pm 1.1$ Dpp for Dpp inflow and $\langle \Delta c_{\mathrm{out}} \rangle = 6.6 \pm 0.6$ Dpp for Dpp outflow. Small steps (< 2 Dpp) are within the noise and explain the dip in the data at $\Delta c_{\mathrm{endo}} = 0$. **c)** Time between fusion events (Dpp inflow). Fitting with a single exponential gives $k_{\mathrm{on}} = 0.75 \pm 0.20\ \mathrm{min}^{-1}$. **d)** Time between off-events (Dpp outflow). Fitting with a single exponential (first order rate reaction) gives $k_{\mathrm{off}} = 1.1 \pm 0.2\ \mathrm{min}^{-1}$.

Dpp. Hence, inflow is characterized by smaller clusters as compared to Dpp outflow. It should be noted that further conclusions based on the shape of the step-size distribution should be drawn with care. The data was taken at different distances to the Dpp source and therefore the distance distribution of the experiments influences the distribution of observed step sizes (more experiments close to the Dpp source will contain more endosomes with high Dpp content and could result in larger step sizes and vice versa). Furthermore, the distribution is slightly biased to larger step sizes. First, small steps (up to a few Dpp) could not be observed because of noise. Secondly, small steps will be more difficult to detect when the endosome fluorescence has significantly bleached. At that moment only a certain fraction of the Dpp in a 'step-event' will be still fluorescent and therefore become more difficult to detect. The bleach-correction algorithm cannot correct for this since it not only increases the fluorescence to original levels, it also increases the noise associated to it.

The difference between the cluster size for Dpp in- and outflow should be reflected in the frequency of these events, provided that both processes are in equilibrium. Therefore, we measured the time between events of the same type (i.e. inflow-inflow and outflow-outflow) using the output of the step-fitting algorithm. The result is plotted for Dpp inflow (fig. 4.11c) and Dpp outflow (fig. 4.11d). Fitting a single exponential yielded $k_{\mathrm{on}} = 0.75 \pm 0.20\ \mathrm{min}^{-1}$ and $k_{\mathrm{off}} = 1.1 \pm 0.2\ \mathrm{min}^{-1}$. The average outflow rate $\langle \Delta c_{\mathrm{out}} \rangle k_{\mathrm{off}} = 7.3$ Dpp/min hence equals (within the margin of error) the average inflow rate $\langle \Delta c_{\mathrm{in}} \rangle k_{\mathrm{on}} = 6.4$ Dpp/min, showing that the system is in a steady state indeed. It should be noted that the distributions in figs. 4.11c,d are probably biased towards longer times, since rapid events involving small changes in Dpp content could not be observed during our experiments.

The obtained values for the in- and outflow rates for individual Dpp are larger than those obtained previously in chapter 3. For the slow limit of intracellular transport (150 s for the whole process) there we found $t_{\mathrm{r,ea}} = 53$ s and $t_{\mathrm{r,r}} = 100$ s for early and recycling endosomes, respectively (with an average $t_{\mathrm{r}} = 77$ s), while here we find $t_{\mathrm{r}} = 8.2$ s. These numbers however do not represent the same parameter of the model. Here we analyzed the time between events, which in itself does not allow us to conclude on the residence time of Dpp in endosomes, which was calculated in chapter 3. The time between events also depends on the number of Dpp in the endosome. The more Dpp in an endosome, the shorter the time between events for the same residence time. Hence, from the difference between the values we can predict that there should be 77/8.2 = 9 Dpp molecules on average per endosome in our experiments.

We found however that the endosomes in which we observed Dpp-concentration changes, had an average Dpp content of 77±7 Dpp molecules. From this we concluded that 88% of the Dpp in endosomes appeared to be immobile on the timescale of our experiments. This immobile fraction of Dpp has been detected before by FRAP experiments, where it was determined to be 62±8% [10]. We suggest that the rest of the difference between the FRAP experiments and our experiments is explained by experimental limitations, which prevented us from seeing small changes in Dpp concentration.

The model presented before (fig. 4.2) contains six events which all could result in the Dpp concentration changes observed. At the same time the model reveals three redundant parameters ($-c_2 = c_3 + c_4$) which involve vesicle transport between endosomes. Therefore they will appear both as up-steps and as down-steps in fig. 4.11b, assuming there is no change in vesicle composition during the transport between endosomes. As a result we rule out events 2, 3 & 4 (i.e. fission of a vesicle containing Dpp from an early endosome which is transported either to a recyling endosome or a late endosome) as possible contributors to the difference between up- and down-steps. The observed difference can therefore only arise from a difference in the number of Dpp molecules that are endocytosed in one step on one hand, and that are recycled and/or degraded on the other hand.

In fig. 4.11d we analyzed the time between fission events. As predicted for a first-order reaction the distribution followed a single-exponential decay. Such first-order reaction (i.e. fission from an early, recycling or late endosome) is summarized in:

$$\text{Endosome} \rightarrow \text{Endosome} + \text{Dpp-vesicle} \tag{4.5}$$

As was shown in chapter 3 the fraction ε of Dpp transferred from an early endosome to a recycling endosome determines the decay length λ of the gradient. Hence, for a well defined gradient it is necessary to keep ε stable. This could be achieved by an active process in the early endosome in which vesicles are predestined to be transferred to a recycling endosome or a late endosome. Since 99.6% of Dpp is transferred to a recycling endosome, in this hypothetical active process, a controlled threshold in Dpp concentration needs to be reached before a vesicle with Dpp leaves the endosome. In a passive process on the other hand the amount of Dpp in the vesicle would be proportional to the Dpp content of the endosome and ε (and hence the gradient) would be statistical.

To distinguish between the two possible processes we calculated the relative step size of all the down-steps. Figure 4.12a shows the distribution of the Dpp concentration in endosomes (C_{endo}) just before an outflow-event took place. The distribution is clearly peaked around 30 Dpp molecules. The distribution of step sizes of the down-steps (dC_{endo}) is shown in fig. 4.12b which shows a resemblance to fig. 4.12a. The latter observation can be best seen in the relative step size $\frac{dC_{\text{endo}}}{C_{\text{endo}}}$ distribution (fig. 4.12c). The distribution is sharply peaked at 0.11, hence in each event 11% of the Dpp content is exchanged. At first sight we concluded from this that the off-events are passive events. However, since the data was slightly biased towards larger step sizes, a fraction of the small relative changes will automatically not appear in fig. 4.12c. Hence, from this data alone we could not rule out that there is still an active process that decides how many Dpp is transferred to a vesicle during a fission event.

Therefore we also analyzed the step sizes versus distance to the Dpp-source. As a consequence of the single exponential distribution of C_{endo} (fig. 4.9a) and a constant relative step size, the absolute step size dC_{endo} should become smaller further away from the source in a passive model. Figure 4.12d shows dC_{endo} as a function of the distance to the source. Fitting a straight line to the data indeed confirmed that dC_{endo} became smaller further away from the source. Fitting a single exponential decay did not significantly improve the fit. Averaging the data (fig. 4.12e) showed that both off-steps and on-steps are smaller further away from the source.

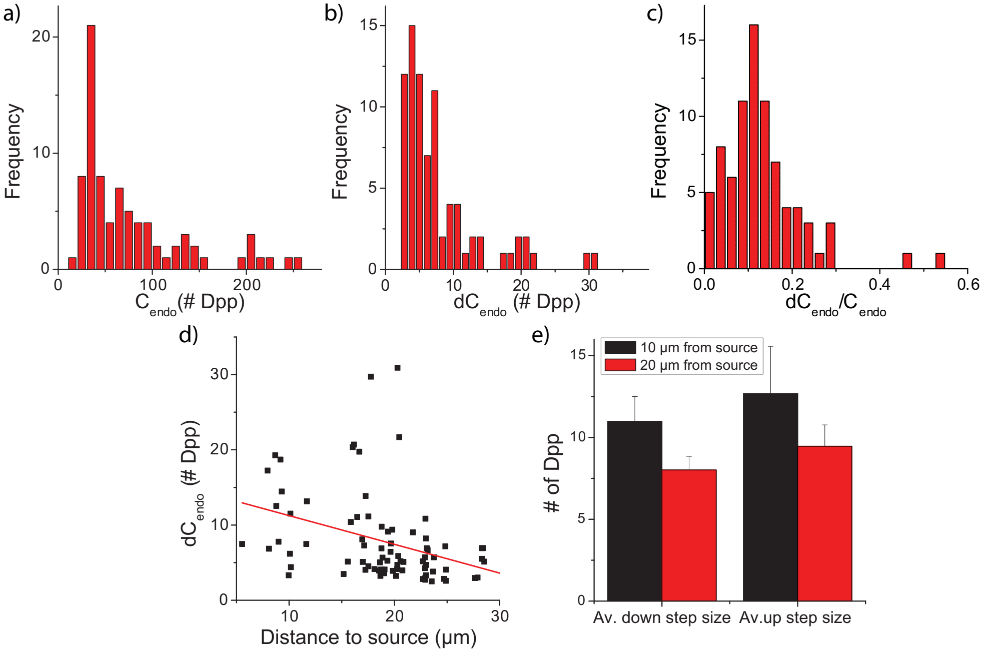

Figure 4.12: **a)** Distribution of Dpp concentration (C_{endo}) in endosomes that undergo an off event. **b)** Distribution of step sizes (dC_{endo}) in off events. **c)** Histogram showing the distribution of relative step sizes ($\frac{dC_{\text{endo}}}{C_{\text{endo}}}$) The distribution is peaked around 0.11. **d)** Step size plotted as a function of distance to the source. The red line shows a fit to the data. **e)** Average step size plotted versus distance to the source for both up and down steps.

4.5 Conclusion

In conclusion we found that the motility of endosomes by itself cannot account for intracellular transport, the observed diffusion constants are too low and almost no lateral active transport occurs. Our observation of regular active transport along the apicobasal axis seems to suggest that endosomal transport takes part in Dpp breakdown.

Static characterization of endosomal Dpp content showed that the number of Dpp-containing endosomes does not vary along the Dpp gradient. The Dpp concentration in those endosomes however becomes smaller further away from the source. From the apicobasal distribution of Dpp endosomes we found that both the number of endosomes and the Dpp content in endosomes is smaller more basally in the tissue.

Intracellular transport of Dpp is governed by small vesicles, which travel between endosomes. Those vesicles contained up to 25 Dpp molecules. Dpp inflow happened in larger cluster sizes than Dpp outflow. From this we concluded that the number of Dpp molecules endocytosed in one step is larger compared to the number of Dpp molecules that is recycled or degraded in one step.

The time between fusion of vesicles with an endosome was about 1 minute on average. A similar value was found for time between fission of vesicles from an endosome. In combination with the results from chapter 3 we found that 88% of Dpp appears to be immobile on the timescale of our experiments, hereby supporting previous FRAP experiments. Control of the vesicle concentration is a result of a passive, probabilistic process.

The quantitative information we obtained on vesicular transport here will have to be integrated in the future into more detailed models to describe the intracellular transport that controls morphogen spreading in tissue and animal development.

Bibliography

[1] Turing, A. *Philos T Roy Soc B* **237**(641):37–72 (1952).

[2] Wolpert, L. *J Theor Biol* **25**(1):1–47 (1969).

[3] Crick, F. *Nature* **225**(5231):420–2 (1970).

[4] Kerszberg, M. and Wolpert, L. *J Theor Biol* **191**(1):103–14 (1998).

[5] Entchev, E., Schwabedissen, A., and González-Gaitán, M. *Cell* **103**(6):981–91 (2000).

[6] González-Gaitán, M. *Nat Rev Mol Cell Biol* **4**(3):213–24 (2003).

[7] Kruse, K., Pantazis, P., Bollenbach, T., Jülicher, F., and González-Gaitán, M. *Development* **131**(19):4843–4856 (2004).

[8] Basler, K. and Struhl, G. *Nature* **368**(6468):208–14 (1994).

[9] Teleman, A. A. and Cohen, S. M. *Cell* **103**(6):971–80 (2000).

[10] Kicheva, A., Pantazis, P., Bollenbach, T., Kalaidzidis, Y., Bittig, T., Jülicher, F., and González-Gaitán, M. *Science* **315**(5811):521–5 (2007).

[11] Bollenbach, T., Kruse, K., Pantazis, P., González-Gaitán, M., and Jülicher, F. *Phys.Rev.Lett.* **94**(1):018103 (2005).

[12] Bollenbach, T., Kruse, K., Pantazis, P., González-Gaitán, M., and Jülicher, F. *Physical Review e* **75**(1):011901 (2007).

[13] Lander, A., Nie, Q., and Wan, F. *Developmental Cell* **2**(6):785–796 (2002).

[14] Lommerse, P. H. M., Vastenhoud, K., Pirinen, N. J., Magee, A. I., Spaink, H. P., and Schmidt, T. *Biophys J* **91**(3):1090–7 (2006).

[15] de Keijzer, S., Sergé, A., van Hemert, F., Lommerse, P. H. M., Lamers, G. E. M., Spaink, H. P., Schmidt, T., and Snaar-Jagaiska, B. E. *Journal of Cell Science* **121**(10):1750–7 (2008).

[16] Nagai, T., Ibata, K., Park, E. S., Kubota, M., Mikoshiba, K., and Miyawaki, A. *Nat Biotechnol* **20**(1):87–90 (2002).

[17] Holtzer, L., Meckel, T., and Schmidt, T. *Applied Physics Letters* **90**(5):053902 (2007).

[18] Harms, G. S., Cognet, L., Lommerse, P. H. M., Blab, G. A., and Schmidt, T. *Biophys J* **80**(5):2396–408 (2001).

[19] Steinmeyer, R., Noskov, A., Krasel, C., Weber, I., Dees, C., and Harms, G. S. *Journal of Fluorescence* **15**(5):707–21 (2005).

[20] Ajo-Franklin, C. M., Drubin, D. A., Eskin, J. A., Gee, E. P. S., Landgraf, D., Phillips, I., and Silver, P. A. *Genes Dev* **21**(18):2271–6 (2007).

[21] Kerssemakers, J. W. J., Munteanu, E. L., Laan, L., Noetzel, T. L., Janson, M. E., and Dogterom, M. *Nature* **442**(7103):709–12 (2006).

[22] Carter, B. C., Vershinin, M., and Gross, S. P. *Biophys J* **94**(1):306–19 (2008).

[23] Huet, S., Karatekin, E., Tran, V., Fanget, I., Cribier, S., and Henry, J. *Biophys J* **91**(9):3542–3559 (2006).

[24] Saxton, M. and Jacobson, K. *Annu.Rev.Biophys.Biomol.Struct.* **26**:373–399 (1997).

[25] González-Gaitán, M. *Mech Dev* **120**(11):1265–82 (2003).

[26] Seisenberger, G., Ried, M. U., Endress, T., Büning, H., Hallek, M., and Bräuchle, C. *Science* **294**(5548):1929–32 (2001).

[27] Kural, C., Kim, H., Syed, S., Goshima, G., Gelfand, V., and Selvin, P. R. *Science* **308**(5727):1469–1472 (2005).